Acta Crystallographica Section D
Biological Crystallography
ISSN 0907-4449

Structural determination of a partially hemihedrally twinned actin crystal

Lakshmanan Govindasamy, Robbie Reutzel, Mavis Agbandje-McKenna and Robert McKenna*

Department of Biochemistry and Molecular Biology, McKnight Brain Institute, University of Florida College of Medicine, Gainesville, Florida 32601, USA

Correspondence e-mail: rmckenna@ufl.edu

Received 21 October 2003
Accepted 23 March 2004

PDB References: actin, 1rfq, r1rfqsf

An orthorhombic actin crystal (space group $P2_12_12_1$, unit-cell parameters a = 101.6, b = 103.0, c = 127.0 Å) was converted into a partially hemihedrally twinned tetragonal crystal (space group $P4_3$, unit-cell parameters $a = b$ = 101.5, c = 104.2 Å) by induced condensation. This condensation (decrease in the c axis) was caused by the flash-freezing of the crystal, with 30% PEG 400 as a cryoprotectant, prior to data collection. Diffraction data for the twinned tetragonal crystal were collected at 100 K to 3.0 Å resolution (99.8% completeness with an R_{sym} of 8.1%) using synchrotron radiation. The hemihedral twinning of the data was observed by self-rotation function analysis and was determined to have a partial twin fraction of 0.376 from intensity statistics. The structure, with two actin molecules in the crystallographic asymmetric unit, was determined by molecular-replacement methods and refined to an R factor of 0.193. As a consequence of the crystal lattice transformation from the orthorhombic $P2_12_12_1$ to the tetragonal $P4_3$ space group, actin–actin contacts were rearranged and an inter-actin dimer disulfide bond (Cys374) observed in the orthorhombic crystal form was broken in the tetragonal crystal form.

1. Introduction

Actin consists of a single polypeptide chain of approximately 375 amino acids (molecular weight of ~42 kDa), depending upon the species and organ from which it is isolated. It is one of the most abundant proteins in eukaryotic cells (Sheterline *et al.*, 1999) and plays essential roles in muscle contraction, motility, mitosis and stabilization of the cytoskeleton. Many of these functions depend upon the capacity of actin to be restructured in a controlled but rapid manner by polymerization, depolymerization, cross-linking and branching (Pollard & Borisy, 2003).

Although much studied, the mechanism of actin polymerization remains controversial in the literature. Biochemical and ultrastructural studies have led to the hypothesis that during polymerization from monomeric actin (G-actin) to filamentous actin (F-actin), the G-actin monomer is converted to a precursor lower dimer (LD) actin (named because of its migration on native gels). The LD-actin precursor has been shown to be an antiparallel actin dimer, stabilized by a disulfide bond between symmetry-related C-terminal cysteine residues (Yarmola *et al.*, 2000; Bubb *et al.*, 2002). This Cys374 residue is highly conserved across species (Sheterline *et al.*, 1999). Actin polymerization to form F-actin is reversible and can be controlled by the addition/removal of salts to a solution of G-actin. This phenomenon is sensitive to the state of either bound ATP or ADP and the speed of the process depends on many cellular factors (Steinmetz *et al.*, 1997; De La Cruz &

Pollard, 1995; De La Cruz *et al.*, 2000). Studies under physiological conditions have shown that LD-actin is incorporated into actin filaments *in vitro* (Steinmetz *et al.*, 1997) and that actin polymerization proceeds by a step size of 5.4 nm, with two actin subunits added to the actin filament at each step (Kuo & McGrath, 2000).

Models based on X-ray crystallographic studies of G-actin and LD-actin, and fiber diffraction and cryo-electron microscopy studies of F-actin provide a means of establishing structure–function relationships for actin restructuring (Kabsch *et al.*, 1990; Holmes *et al.*, 1990; Lorenz *et al.*, 1993; Rayment *et al.*, 1993; Bubb *et al.*, 2002; Reutzel *et al.*, 2004).

Here, we discuss the methods by which the observed X-ray diffraction data for a tetragonal $P4_3$ actin crystal were successfully detwinned. The resultant structure determination demonstrated that the flash-freezing condensation shrinkage of the *c* axis by 18% and the possible exposure to synchrotron radiation induced lattice distortions that altered the LD actin–actin crystal contacts and caused the breakage of the Cys374 disulfide bond.

2. Experimental

2.1. Crystallization

The purification of rabbit actin has been described previously (Spudich & Watt, 1971). Crystals of the polylysine–actin–latrunculin A–ATP complex were grown at 277 K using the hanging-drop vapor-diffusion method (McPherson, 1982). A 10 µl crystallization droplet was formed by mixing a solution of equimolar components of actin and latrunculin A at a concentration of 240 µ*M* with 120 µ*M* polylysine in crystallization buffer [1.3 *M* $(NH_4)_2SO_4$, 3.0 m*M* $MgCl_2$, 60 m*M* imidazole pH 6.7]. The droplet was suspended over 1 ml of the crystallization buffer. Useful diffraction-quality crystals appeared after 2–4 weeks (Bubb *et al.*, 2002).

2.2. Data collection and processing

A crystal similar to those that had previously been shown to have a primitive orthorhombic lattice with unit-cell parameters $a = 101.6$, $b = 103.0$, $c = 127.0$ Å when X-ray diffraction data were collected at room temperature (Bubb *et al.*, 2002) was soaked for approximately 30 s in a solution identical to the crystallization buffer but containing 30%(*v*/*v*) PEG 400 as a cryoprotectant and flash-frozen to 100 K.

A single frozen crystal was used for data collection on the A1 beamline at the Cornell High Energy Synchrotron Source using a Quantum 4 CCD detector system. The crystal-to-detector distance was 150 mm and a 1.0° oscillation angle per image was used. A total of 150 images were collected with an exposure time of 60 s per image. The data collected had a maximum useable diffraction limit of 3.0 Å resolution. All images were indexed, integrated and scaled with the *HKL* suite programs *DENZO* and *SCALEPACK* (Otwinowski & Minor, 1997).

2.3. Structure solution and refinement

The hemihedral twinning was characterized using the intensity statistics and distributions obtained from the *TRUNCATE*, *DETWIN* (Collaborative Computational Project, Number 4, 1994) and *CNS* (Brünger *et al.*, 1998) programs. The self-rotation function calculations were performed on data between 10 and 4 Å resolution using the *POLARRFN* program (Collaborative Computational Project, Number 4, 1994). The structure of actin in the $P4_3$ crystal form was solved entirely using the twinning procedures and was refined with simulated-annealing, individual *B*-factor and energy-minimization procedures using the *CNS* software (Brünger *et al.*, 1998) interspersed with rounds of manual model building with the graphics program *O* (Jones, 1978). The quality of the final refined structure was validated with the *PROCHECK* (Laskowski *et al.*, 1993) and *CNS* (Brünger *et al.*, 1998) programs.

Least-squares superimpositions of the actin structures determined in the $P4_3$ and $P2_12_12_1$ crystal forms were performed using the program *O* (Jones, 1978). Figs. 3 and 4 were generated with the program *BOBSCRIPT* (Esnouf, 1999).

3. Results and discussion

3.1. Space-group assignment

Initially, because of the previously recorded diffraction data collected for actin crystals grown as described in §2, the cryo-collected diffraction data were indexed in the orthorhombic Laue group *P*222, with unit-cell parameters $a = 101.5$, $b = 101.5$, $c = 104.2$ Å. Immediately apparent from the unit-cell parameters was the drastic ∼18% reduction in the *c* axis from $c = 127.0$ Å for crystals obtained using the same crystallization conditions but for which the data were collected at room temperature (Bubb *et al.*, 2002). Also observed, but less dramatic, was that the unit-cell parameters *a* and *b* were now identical for this new crystal form. The observed Bragg diffraction pattern appeared to be ordered and all reflections were predicted based on the unit-cell parameters. Furthermore, the frozen crystal diffracted X-rays to higher resolution (3.0 Å resolution) compared with those for which data were collected at room temperature (3.5 Å resolution). This may have been more a consequence of using synchrotron radiation for data collection compared with an in-house home source, rather than the change in crystal form.

Therefore, because of the possible ambiguity in Laue group assignment, the diffraction images were re-indexed using experimental parameters derived from processing the data set as *P*1 and integrated and scaled as the tetragonal *P*4, *P*422 and the orthorhombic *P*222 Laue groups. This resulted in $R_{\rm sym}$ values of 0.081, 0.141 and 0.129, respectively. The predicted reflections for all three crystal system settings fitted the observed data equally well. Table 1 gives the data-processing statistics for all three Laue group assignments. The significantly lower $R_{\rm sym}$ value indicated that the crystal system might be *P*4 and that the observed pseudo-twofold crystallographic

Table 1
Data-processing statistics assuming *P*4, *P*422 and *P*222 Laue groups.

	*P*4			*P*422			*P*222		
Resolution (Å)	No. reflections	R_{sym}†	Completeness (%)	No. reflections	R_{sym}†	Completeness (%)	No. reflections	R_{sym}†	Completeness (%)
50.0–6.46	2166	0.049	99.6	1253	0.100	99.5	2246	0.089	95.5
6.46–5.13	2131	0.058	99.9	1161	0.123	99.9	2177	0.110	97.5
5.13–4.48	2112	0.068	99.8	1144	0.132	100.0	2168	0.120	98.1
4.48–4.07	2110	0.080	100.0	1128	0.153	99.9	2148	0.145	98.5
4.07–3.78	2079	0.096	99.9	1111	0.164	100.0	2136	0.153	98.8
3.78–3.56	2139	0.119	99.9	1135	0.180	100.0	2154	0.170	99.0
3.56–3.38	2075	0.166	99.8	1101	0.230	100.0	2138	0.221	99.1
3.38–3.23	2095	0.213	100.0	1104	0.274	100.0	2123	0.266	99.2
3.23–3.11	2117	0.380	100.0	1115	0.435	100.0	2136	0.362	99.1
3.11–3.00	2071	0.408	99.8	1089	0.477	100.0	2133	0.525	99.1
Overall	21085	0.081	99.8	11341	0.141	99.9	21559	0.129	98.4

† $R_{sym} = \sum |I_{obs} - I_{avg}| / \sum I_{obs}$, where the summation is over all reflections.

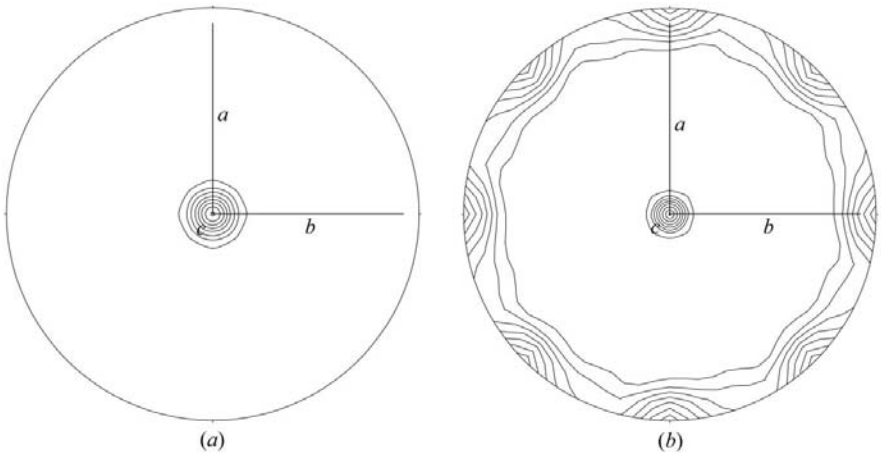

Figure 1
Self-rotation function stereographic projections of the *P*4 reduced data set for (*a*) the $\kappa = 90^\circ$ section and (*b*) the $\kappa = 180^\circ$ section calculated for data between 10 and 4 Å resolution using the *POLARRFN* program (Collaborative Computational Project, Number 4, 1994).

symmetry may be caused by a non-crystallographic symmetry (NCS) actin dimer (LD-actin) in the crystal lattice.

Matthews coefficients V_M (Matthews, 1968) were also calculated for the three crystal systems, assuming the molecular weight of G-actin to be 42 kDa. The V_M value for all three Laue groups was ~3.6, assuming one G-actin molecule per asymmetric unit for the crystal system *P*422 and two G-actin molecules per asymmetric unit for the crystal systems *P*222 and *P*4. Therefore, neither the orthorhombic nor the tetragonal crystal systems could be eliminated based on these calculations.

Self-rotation function calculations (Rossmann & Blow, 1963) for kappa (κ) set at 90 and 180° were performed using data between 10 and 4 Å resolution. Fig. 1 shows self-rotation function results for the *P*4 crystal system; similar results were observed for the other two crystal systems (data not shown). For $\kappa = 90^\circ$ a single strong peak parallel to the *c* axis (characteristic of a fourfold crystallographic axis) was observed, whereas for $\kappa = 180^\circ$ twofold rotation axes were observed parallel to the *a* and *b* axes and to the diagonal between them. The interpretation of the $\kappa = 90$ and 180° rotation-function results taken together for all three crystal systems gave the impression that the crystal system had a crystallographic fourfold symmetry axis parallel to the *c* axis with only pseudo-422 symmetry, the actin–actin NCS dimer twofold being masked by the pseudo-422 crystal symmetry, as the NCS twofold was diagonal to the *a* and *b* crystallographic axes. The assignment of Laue group *P*4 was also in agreement with the observed R_{sym} values (Table 1). The space group was therefore assigned as $P4_1$ or $P4_3$ based on possible packing arrangements and inspection of the 00*l* reflections, which showed a clear indication of a screw axis along *c*.

3.2. Structure solution

3.2.1. Initial structure solution assuming no crystal twinning. The structure of actin in the *P*4 crystal form was initially determined with the assumption that the space group was either $P4_1$ or $P4_3$, but without the consideration that the data might be twinned. This procedure used standard molecular-replacement protocols (Rossmann, 1990) using a G-actin monomer (PDB code 1lcu) as the search model in the *CNS* program package (Brünger *et al.*, 1998). The results below are only given for the $P4_3$ space group, as it was evident that there were no solutions assuming $P4_1$ as the space group. Cross-rotation function calculations carried out with data between 30 and 4 Å resolution yielded two unambiguous non-crystallographic symmetry (NCS) solutions (solution *A*, $\theta_1 = 357.3$, $\theta_2 = 10.9$, $\theta_3 = 3.4^\circ$; solution *B*, $\theta_1 = 154.5$, $\theta_2 = 167.2$, $\theta_3 = 151.9^\circ$). A translation search orientating the G-actin monomer using solution *A* gave a position of $T_x = -26.0$, $T_y = 40.1$ and $T_z = 0.9$ Å. This monomer was then positioned in the unit cell and the position of the second monomer was then determined, using the orientation of solution *B*, to be $T_x = -8.1$, $T_y = 9.3$ and $T_z = 85.9$ Å. The combined correlation coefficient for the two NCS-related monomers was 0.55, with a packing value of 0.46. This solution was refined with cycles of

simulated-annealing, individual *B*-factor and energy-minimization procedures in *CNS* (Brünger *et al.*, 1998) interspersed with rounds of manual model building using the program *O* (Jones, 1978), but the R_{work} and R_{free} values did not converge to less than 32 and 36%, respectively. These results called for a re-examination of the assigned space group and data processing and the possibility that the diffraction data were twinned.

3.2.2. Detection of twinning. Generally, two distinct types of twinning effects can occur in crystals, either during crystal growth (probably not the case in this situation), where the crystal is composed of two completely different species orientations, or when some sort of stress is applied to a crystal and the twinning is the product of a polymorphic transformation. An example of this induced deformation twinning is caused during the flash-freezing of a crystal to cryogenic temperatures (the most likely event that occurred in this case) (Yeates, 1997). During data processing, no split reflections that would suggest epitaxial twinning were observed. This indicated that if the data were twinned it would be a case of hemihedral twinning (a type of merohedral twinning), in which the diffraction patterns of the twin domains are completely superimposed on each other. The first sign of possible hemihedral twinning was the observation that the diffraction data could be indexed, integrated and scaled with good overall R_{sym} values in the *P*4 Laue group, but only reasonably well (especially in the lower resolution shells) in

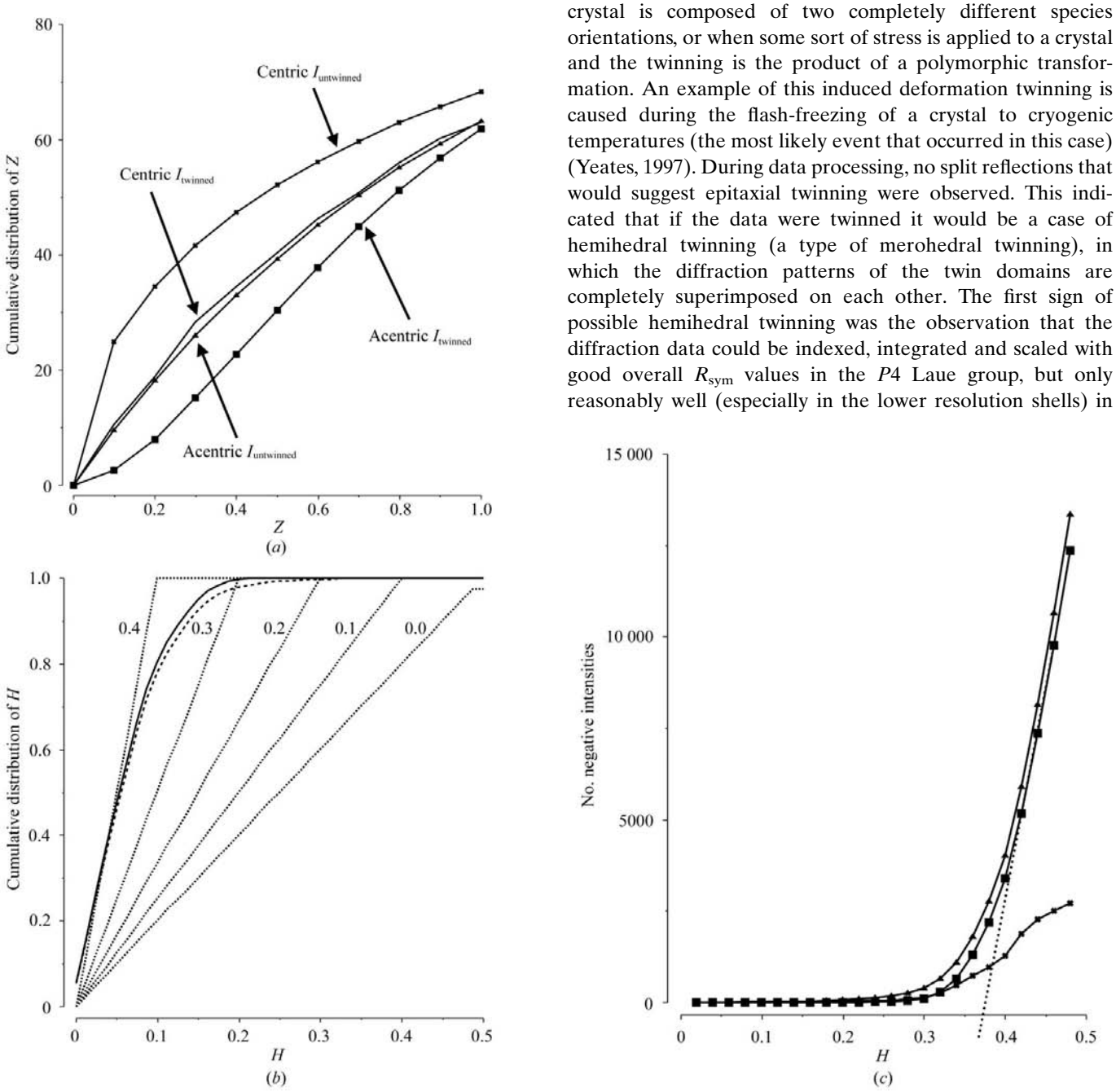

Figure 2
Estimation of the twinning fraction (α) of the reduced *P*4 data set. (*a*) Cumulative intensity $N(z)$ distribution plot, where $N(z)$ is the percentage of reflections with $I/\langle I\rangle$ less than or equal to Z. Shown is the distribution for centric and acentric $I_{twinned}$ for the *P*4 reduced data set and $I_{untwinned}$, the theoretical distribution of untwinned data. The sigmoid-shaped distribution of the acentric reflections for the *P*4 data is characteristic of hemihedral twinning, with an inferred calculated value α of 0.37. (*b*) Estimation of α by plotting the cumulative fractional intensity difference between acentric twin-related intensities, $H = |I_{twinh1} - I_{twinh2}|/(I_{twinh1} + I_{twinh2})$, as a function of H. $I_{twinh1} - I_{twinh2}$ are the intensities of two reflections related by the twin operator before detwinning. The solid line shows the *P*4 reduced data and the dotted lines show the expected values for the twin fractions 0.0, 0.1, 0.2, 0.3 and 0.4. The initial slope of the distribution is a measure of α (Yeates, 1988). (*c*) Estimation of α by Britton plots (Britton, 1972; Fisher & Sweet, 1980). The number of negative intensities after detwinning is plotted as a function of the assumed twinning fraction. An overestimation of α will increase the number of the negative intensities and the actual value of α is extrapolated from this increase (dotted lines). (*a*) was generated using the program *TRUNCATE* and (*b*) and (*c*) using *DETWIN* (Collaborative Computational Project, Number 4, 1994).

the *P*422 and *P*222 Laue groups. Table 1 shows the resolution-dependence of R_{sym}. The overall R_{sym} does not give a clear indication that the data is twinned, whereas the R_{sym} values in the lower resolution shells (50.0–4.0 Å resolution) were nearly a factor of two larger for the data scaled as *P*422 or *P*222 compared with *P*4. This is a useful indicator that the data is twinned, as the apparently higher symmetry may arise from the twin operator and therefore introduce symmetry that is not part of the Laue symmetry of the space group. Another way to observe signs of hemihedral twinning in a data set is to plot its cumulative intensity distribution. Fig. 2(*a*) shows the calculated cumulative distribution of intensity for the reduced *P*4 data using the software *TRUNCATE* (Collaborative Computational Project, Number 4, 1994). The plot profile for the acentric reflections is sigmoidal in shape compared with the plot of the theoretical standard curve distribution of untwinned data (Stanley, 1972; Yeates, 1997; Breyer *et al.*, 1999). This plot profile for the reduced *P*4 data indicates that there are far less weaker acentric reflections in the data set than are generally observed for untwinned data. A comparison of the cumulative intensity distribution of the reduced *P*4 data set to standard untwinned data showed that there was a high degree of twinning, with an estimated twinning fraction (α) of 0.37. This observed distribution added further supporting evidence that the data were indeed twinned. To fully assess the twin fraction of the observed data, two additional twinning tests were employed using the programs *CNS* (Brünger *et al.*, 1998) and *DETWIN* (Collaborative Computational Project, Number 4, 1994). For acentric perfectly twinned data, the expected ratio of the average squared intensity to the square of the average intensities, $\langle I^2\rangle/\langle I\rangle^2$, is 1.5, whereas for untwinned data this value is 2.0. For the data set reduced as *P*4 this value was 1.69. In a similar way, the Wilson ratio $\langle E^2\rangle/\langle E\rangle^2$, where E is the normalized structure factor, is expected to give a value of 0.785 for perfectly twinned data and 0.885 for untwinned data. For the *P*4 data set this value was 0.857. Both these ratios therefore gave a strong indication that the crystal was partially hemihedrally twinned (Yeates, 1988).

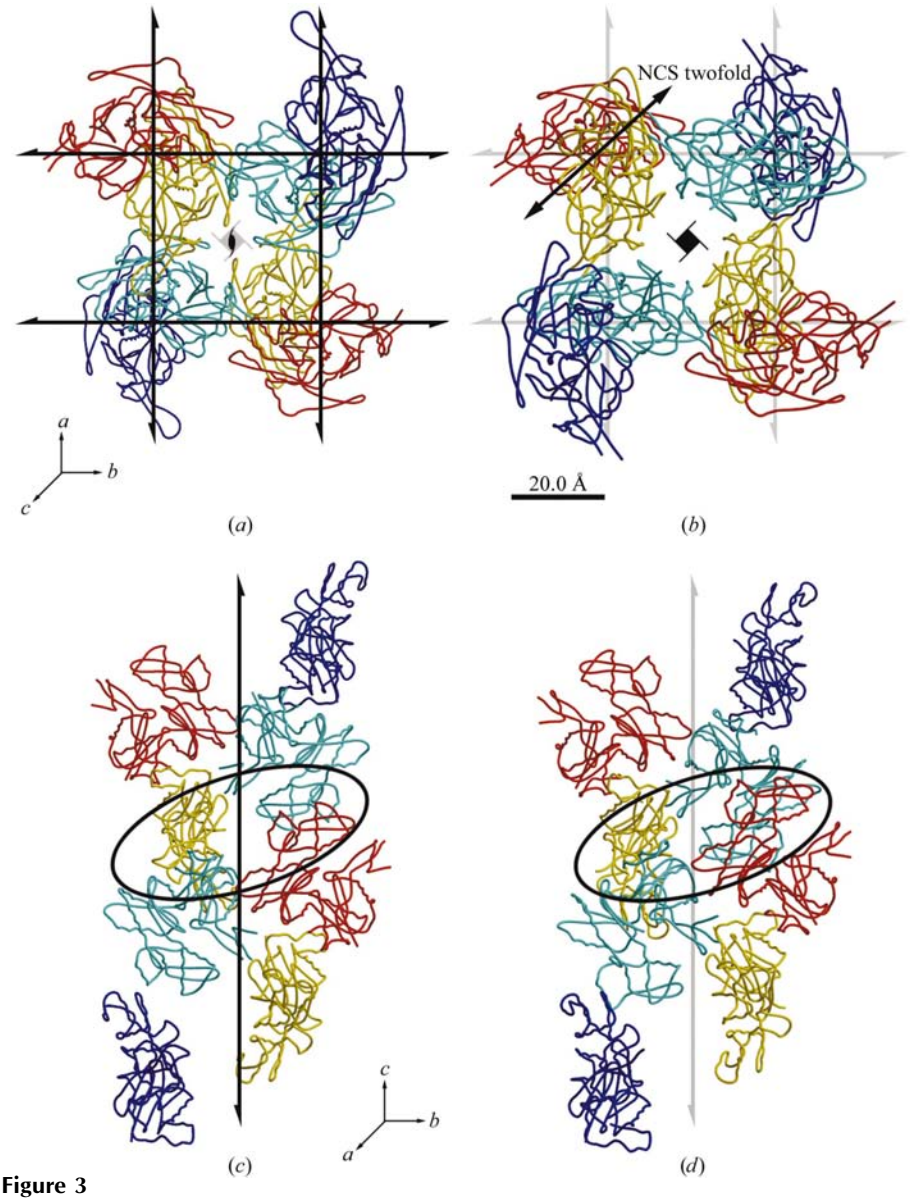

Figure 3
Actin packing in the $P2_12_12_1$ and $P4_3$ crystal lattices. Crystal lattice packing diagrams viewed (*a*) and (*b*) down the *c* axes, and (*c*) and (*d*) down the *a* axes of the $P2_12_12_1$ and $P4_3$ crystal forms, respectively. Four actin antiparallel dimers (LD-actin) are shown. The LD-actin molecules are depicted as either orange and yellow or blue and cyan pairs. (*a*) and (*b*) Note the pseudo-twofold and fourfold symmetry in the $P2_12_12_1$ and $P4_3$ crystal forms (crystallographic and pseudosymmetry shown as black and gray lines, respectively). Also shown is the direction of the non-crystallographic symmetry axis within one of the LD-actin molecules. (*c*) and (*d*) The open ellipsoids show the relative compression of the *c* axis in the $P4_3$ compared with the $P2_12_12_1$ crystal form. The LD-actin molecules slide over each other, decreasing the *c* axis by ∼23 Å.

The twin fraction (α) was also determined using two other methods. A plot (Fig. 2*b*) of the cumulative distribution of H, where H is defined as $H = |I_{twinh1} - I_{twinh2}|/(I_{twinh1} + I_{twinh2})$ and I_{twinh1} and I_{twinh2} are the observed intensities of two acentric reflection related by a twin law (in this case, the point-group *P*4 relationship where h, k, l is related to $h, -k, -l$), allows α to be estimated directly from the relationships $\langle H\rangle = \frac{1}{2} - \alpha$ and $\langle H^2\rangle = (1 - 2\alpha)^2/3$ (Yeates, 1988). Similarly, a plot (Fig. 2*c*) of the number of negative reflections accumulated after detwinning a data set against α (Britton plot; Britton, 1972) can be used to extrapolate the value of α of a data set. The mean value of α was determined using the software *DETWIN* (Collaborative Computa-

tional Project, Number 4, 1994) and was directly calculated from the *H* and the Britton plots to be 0.37 and 0.39, respectively. Based on the determined values for the twin fraction, the *P*4 data were assigned a mean twinning fraction of 0.376 applying the twin operator $(h, -k, -l)$.

Table 2
Refinement statistics for the $P4_3$ actin crystal structure.

Values in parentheses are for the outer resolution shell.

Data collection	
Unit-cell parameters (Å)	a = 101.5, c = 104.2
Resolution limit (Å)	3.0 (3.11–3.0)
Wavelength (Å)	0.9290
R_{sym}†	0.081 (0.408)
Measured reflections	274846
Unique reflections	21085
Multiplicity/redundancy	13.0 (7.2)
Completeness (%)	99.8 (99.8)
$I/\sigma(I)$	12.32
$I > 3\sigma(I)$	18967
Matthews coefficient (Å^3 Da^{-1})	3.6
Solvent content (%)	64.5
Model refinement	
R factor‡	0.193 (0.342)
R_{free}§	0.261 (0.387)
PDB code	1rfq
No. residues	365 (chain A/B)
No. water molecules	44
Average B value (Å^2)	63.4
R.m.s.d. bonds (Å)	0.01
R.m.s.d. angles (°)	1.5
Ramachandran plot	
Most favored	374 (59.7%)
Additionally allowed	248 (39.6%)
Generously allowed	3 (0.5%)
Disallowed	1 (0.2%)

† $R_{sym} = \sum|I_{obs} - I_{avg}|/\sum I_{obs}$, where the summation is over all reflections. ‡ R factor $= \sum|F_{obs} - F_{calc}|/\sum F_{obs}$. § 5% of reflections were reserved for calculation of R_{free}.

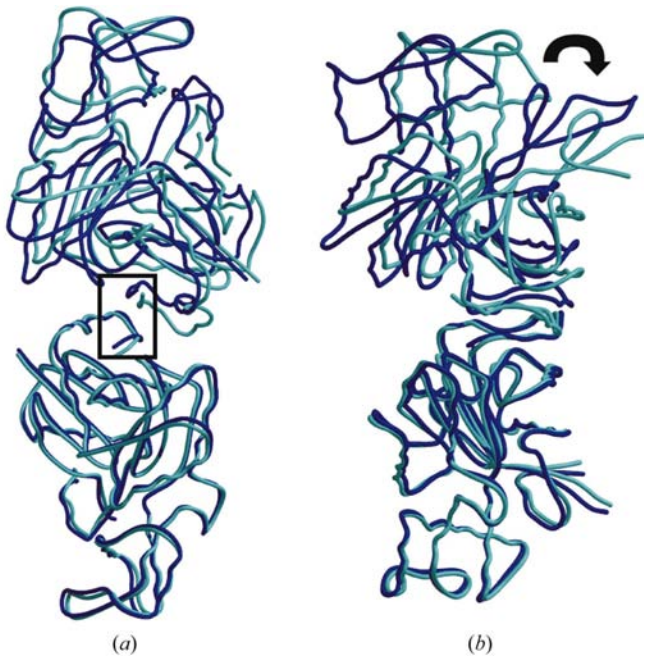

Figure 4
Actin antiparallel dimer (LD-actin). Structural overlay of the LD-actin in the $P4_3$ (cyan) and $P2_12_12_1$ (blue) crystal forms. Viewed (*a*) about the non-crystallographic twofold and (*b*) a 90° rotation. Only one actin monomer (bottom monomer in *a* and *b*) of each LD-actin molecule is superimposed (r.m.s.d. 1.5 Å). Note the relative ∼20° clockwise rotation within the LD-actin pairs (upper monomer in *b*) between the $P2_12_12_1$ and $P4_3$ crystal forms.

3.2.3. Structure solution assuming hemihedral twinning. The previously described $P4_3$ structure solution (which converged to an R_{work} of 32% without taking into account that the data was twinned) was further refined within the *CNS* software package using the twinning fraction and the twinning operator $(h, -k, -l)$. The self-rotation function was re-interpreted and the two twofold symmetry operators seen along the *a* and *c* axes were found to be a function of the twin operator (Fig. 1). After one cycle each of rigid-body, individual *B*-factor and energy-minimization refinement (allowing the two NCS-related actin molecules to be refined independently of each other) the twinned R_{work} and R_{free} values decreased to 25.2 and 26.3%, respectively. The improvement of these parameters was concomitant with significant improvement in the quality of the calculated electron-density maps. On inspection of $2F_o - F_c$ and $F_o - F_c$ electron-density maps, some actin side chains were repositioned and the ATP and latrunculin A molecules and an Mg^{2+} ion were identified and positioned using the molecular-graphics program *O* (Jones, 1978). The ATP and latrunculin A molecular geometries were obtained from the HIC-UP database (Kleywegt & Jones, 1998). Refinement and model building continued for several more cycles until convergence of the R_{work} and R_{free} values. In the final stage of refinement, solvent molecules were included in positive electron density at the 1.5σ level using the automatic water-picking protocol in the *CNS* (Brünger *et al.*, 1998) program. The final refined structure contained the LD-actin, each monomer consisting of 365 amino-acid residues (ten amino acids in the DNase loop were disordered), ATP, latrunculin A an Mg^{2+} ion and 44 ordered water molecules, with a final R factor of 0.193 and R_{free} of 0.261. Details of the refinement statistics are listed in Table 2 and in the supplementary material.[1]

3.3. Comparative analysis of the orthorhombic $P2_12_12_1$ and tetragonal $P4_3$ crystal forms

The most significant difference between the orthorhombic $P2_12_12_1$ and the tetragonal $P4_3$ crystal systems was a shrinkage of the *c* axis by ∼23 Å (Fig. 3). The shortening of this unit-cell parameter and the space-group transformation were presumably mediated by dehydration owing to exposure of the crystal to a cryoprotectant. Dehydration events when subjecting crystals to high concentrations of glycerol have been documented and indeed have been used to gain higher resolution diffraction (Heras *et al.*, 2003). Fig. 3 shows the packing arrangement of the actin molecules in both crystal forms. The lattice transformation is shown from the pseudo-fourfold axis of the orthorhombic system (Fig. 3*a*) to the crystallographic fourfold axis of the tetragonal form (Fig. 3*b*). While the molecular packing looks similar down the *c* axis, Figs. 3(*c*) and

[1] Supplementary data have been deposited in the IUCr electronic archive (Reference: EA5010). Details for accessing these data are given at the back of the journal.

3(*d*) show the extent of the lattice collapse along the *c* axis within the tetragonal crystal and the new interactions that have been formed. The major consequence of this *c*-axis collapse is the formation of a new actin-dimer interface in the $P4_3$ crystal lattice between residues 221–236 of symmetry-related actin monomers (Fig. 3*d*). This new crystal interface involves extensive hydrogen-bonding interactions that may stabilize the $P4_3$ crystal lattice and could be the possible cause of the increased resolution of diffraction of the tetragonal crystal form (3.0 Å) compared with that of the orthorhombic crystal form (3.5 Å).

The observed lattice rearrangements were either caused by or were the cause of a more subtle difference between the LD-actins that exist in both crystal forms. Bubb *et al.* (2002) showed that within the orthorhombic crystal system, the so-called DNase I loop (residues 41–52) from subdomain II of the G-actin monomer makes contacts with a symmetry-related LD-actin interface. The residues making this interaction are well ordered and form a trimer between the LD-actin and another actin monomer comprised of mainly electrostatic interactions. This interaction occurs with only one monomer of each of the LD-actins, the other monomer's DNase I loop being disordered. An examination of the actin-molecule structures in the tetragonal crystal form shows that neither LD-actin monomer's DNase I loop are ordered and, as such, there are no clear contacts forming a trimer.

Least-squares superimposition in the program *O* (Jones, 1978) of one monomer of the LD-actin from the orthorhombic crystal onto the corresponding monomer of this dimer from the tetragonal crystal revealed an r.m.s. deviation of ∼1.5 Å for the C^{α} atoms (treating each monomer as a rigid body). This superimposition of the LD-actins from both crystal forms also highlighted the relative differences in rotation and translation between the actin momomers that form this actin antiparallel dimer (Fig. 4). The transformation that describes this difference in the actin–actin dimer formations is

$$\begin{pmatrix} 0.9582 & -0.1012 & 0.2678 \\ 0.0476 & 0.9787 & 0.1995 \\ 0.2823 & 0.1784 & 0.9426 \end{pmatrix} + \begin{pmatrix} -1.2489 \\ -7.2288 \\ -14.7836 \end{pmatrix}.$$

This movement is attributed to the flexibility around the disulfide bond and the subsequent cleavage of this bridge between the monomers that form the LD-actin (Fig. 5). It is still unclear as to what has caused the shearing of this disulfide bond that forms the LD interaction. Studies of radiation damage caused by synchrotron data collection have showed that with intense X-ray beams highly specific features such as cleavage of disulfide bonds, loss of density for some ionizable side chains and an overall increase in atomic *B* factors can occur (Burmeister, 2000; Leiros *et al.*, 2001). Figs. 5(*a*) and 5(*b*) show stereoviews of the two LD-actin interfaces found in the orthorhombic and tetragonal space groups.

The disulfide bridge between the monomers in the LD-actin for the orthorhombic form is 2.03 Å (Fig. 5*a*), whereas in the tetragonal form the cysteine residues are 6.5 Å apart (Fig. 5*b*).

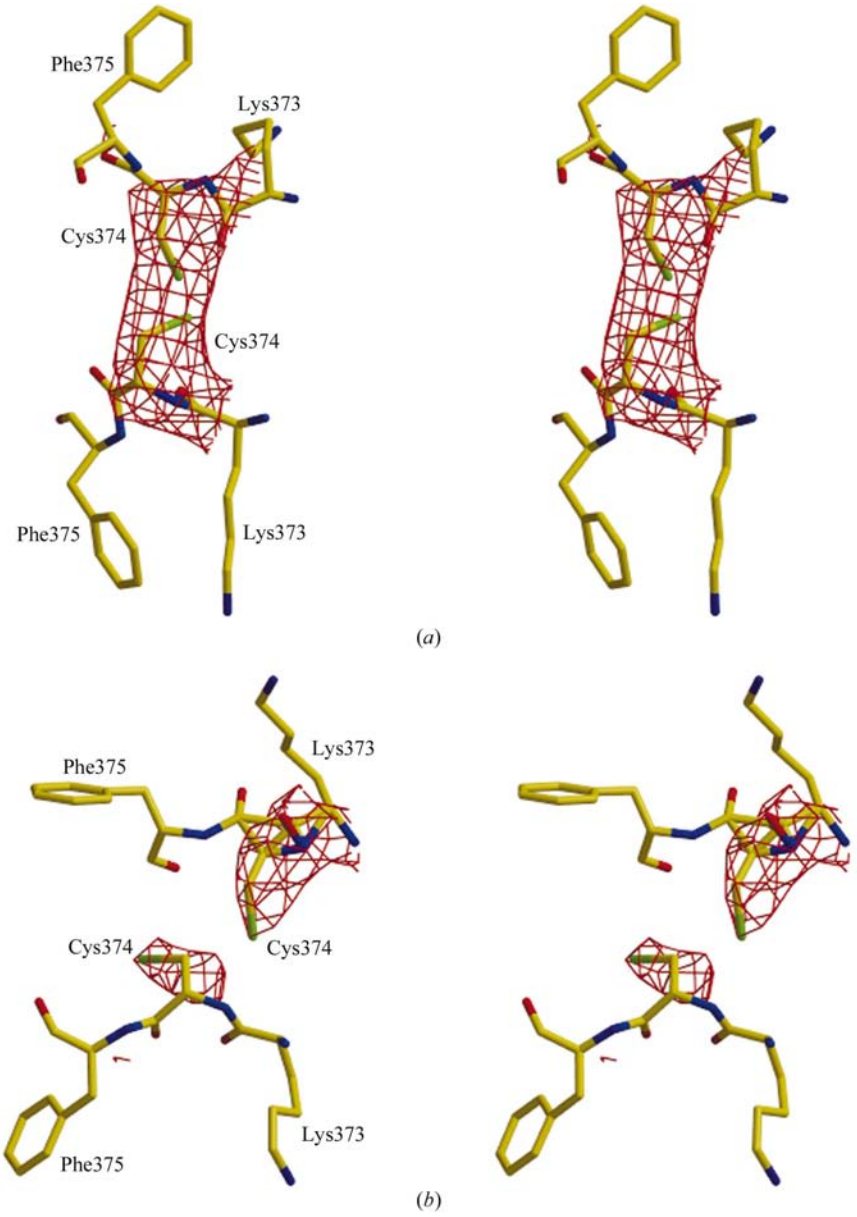

Figure 5
Close-up stereoview of the (*a*) $P2_12_12_1$ and (*b*) $P4_3$ actin antiparallel dimer interface, depicted as viewed in the open rectangle drawn in Fig. 4(*a*). Residues Lys373, Cys374 and Phe375 are shown as a ball-and-stick representation. Electron density (red) is shown as a $2F_o - F_c$ map contoured at 2σ for residue Cys374. Note the break of the disulfide bond in the $P4_3$ crystal form.

This breakage of the disulfide link appears to have allowed the displacement of one monomer within the LD-actin in the tetragonal crystal form. Whether this cleavage was mediated by a rheological twisting of the dimer at the disulfide bridge remains a mystery. It is important to note, however, that synchrotron radiation has been known to cause specific radiation damage in crystals, including the breaking of disulfide bonds (Weik *et al.*, 2000; Sliz *et al.*, 2003). The high average *B* factor observed in this structure (63.4 Å^2) may also be a sign of radiation damage caused by synchrotron radiation (Leiros *et al.*, 2001). Interestingly, the average *B* factor for the original orthorhombic LD-actin model was 62.4 Å^2 and this data was collected on a home-source rotating-anode generator at room temperature (Bubb *et al.*, 2002). Both of these crystal forms also have a higher than normal solvent content (70.6% for the orthorhombic and 64.5% for the twinned tetragonal form) that may cause an inherent degree of lattice disorder. While this may be the case, it is unlikely that a crystal with a large amount of radiation damage would diffract to higher resolution than the native form. Reutzel *et al.* (2004) speculate that this disulfide cleavage may be biologically analogous to the last step in F-actin elongation by LD-actin, resulting in the dissociation of one of its monomers from the filament.

The circumstances of this crystal dehydration shows that while molecules are stabilized in a crystal lattice, they are still able to display dynamic behaviors that may occur *in vivo*. The structural basis of F-actin dynamics is very difficult to study because of the inability to locate and purify polymerization intermediates. Nonetheless, by mimicking the condensation conditions of F-actin nucleation in a crystal lattice it has been possible to 'trap' possible intermediate species of actin polymerization.

The authors wish to thank Elena Yarmola and Michael Bubb for useful discussion on the biological significance of this research to actin function and dynamics, and MacCHESS staff for help provided during data collection. This work was supported by a College Incentive Fund from the University of Florida College of Medicine (RM).

References

Breyer, W. A., Kingston, R. L., Anderson, B. F. & Baker, E. N. (1999). *Acta Cryst.* D**55**, 129–138.
Britton, D. (1972). *Acta Cryst.* A**28**, 296–297.
Bubb, M. R., Govindasamy, L., Yarmola, E. G., Vorobiev, S. M., Almo, S. C., Somasundaram, T., Chapman, M. S., McKenna, M. A. & McKenna, R. (2002) *J. Biol. Chem.* **277**, 20999–21006.
Burmeister, W. P. (2000). *Acta Cryst.* D**56**, 328–341.
Brünger, A. T., Adams, P. D., Clore, G. M., DeLano, W. L., Gros, P., Grosse-Kunstleve, R. W., Jiang, J.-S., Kuszewski, J., Nilges, M., Pannu, N. S., Read, R. J., Rice, L. M., Simonson, T. & Warren, G. L. (1998). *Acta Cryst.* D**54**, 905–921.
Collaborative Computational Project, Number 4 (1994). *Acta Cryst.* D**50**, 760–763.
De La Cruz, E. M., Mandinova, A., Steinmetz, M. O., Stoffler, D., Aebi, U. & Pollard, T. D. (2000). *J. Mol. Biol.* **295**, 517–526.
De La Cruz, E. M. & Pollard, T. D. (1995). *Biochemistry*, **34**, 5452–5461.
Esnouf, R. M. (1999). *Acta Cryst.* D**55**, 938–940.
Fisher, R. G. & Sweet, R. M. (1980). *Acta Cryst.* A**36**, 755–760.
Heras, B., Edeling, M. A., Byriel, K. A., Jones, A., Raina, S. & Martin, J. L. (2003). *Structure*, **11**, 139–145.
Holmes, K. C., Popp, D., Gebhard, W. & Kabsch, W. (1990). *Nature (London)*, **347**, 44–49.
Jones, T. A. (1978). *J. Appl. Cryst.* **11**, 268–272.
Kabsch, W., Mannherz, H. G., Suck, D., Pai, E. F. & Holmes, K. C. (1990). *Nature (London)*, **347**, 37–44.
Kleywegt, G. J. & Jones, T. A. (1998). *Acta Cryst.* D**54**, 1119–1131.
Kuo, S. C. & McGrath, J. L. (2000). *Nature (London)*, **407**, 1026–1029.
Laskowski, R. A., MacArthur, M. W., Moss, D. S. & Thornton, J. M. (1993). *J. Appl. Cryst.* **26**, 283–291.
Leiros, H. S., McSweeney, S. M. & Smalas, A. O. (2001). *Acta Cryst.* D**57**, 488–497.
Lorenz, M., Popp, D. & Holmes, K. C. (1993). *J. Mol. Biol.* **234**, 826–836.
McPherson, A. (1982). *The Preparation and Analysis of Protein Crystals.* New York: John Wiley & Sons.
Matthews, B. W. (1968). *J. Mol. Biol.* **33**, 491–497.
Otwinowski, Z. & Minor, W. (1997). *Methods Enzymol.* **276**, 307–326.
Pollard, T. D. & Borisy, G. G. (2003). *Cell*, **112**, 453–465.
Rayment, I., Holden, H. M., Whittaker, M., Yohn, C. B., Lorenz, M., Holmes, K. C. & Milligan, R. A. (1993). *Science*, **261**, 58–65.
Reutzel, R., Yoshioka, C., Govindasamy, L., Yarmola, E., Agbandje-McKenna, M., Bubb, M. & McKenna, R. (2004). In the press.
Rossmann, M. G. (1990). *Acta Cryst.* A**46**, 73–82.
Rossmann, M. G. & Blow, D. M. (1963). *Acta Cryst.* **16**, 39–45.
Sheterline, P., Clayton, J. & Sparrow, J. C. (1999). *Actin*, 4th ed. Oxford University Press.
Sliz, P., Harrison, S. C. & Rosenbaum, G. (2003). *Structure*, **11**, 13–19.
Spudich, J. A. & Watt, S. (1971). *J. Biol. Chem.* **246**, 4866–4871.
Stanley, E. (1972). *J. Appl. Cryst.* **5**, 191–194.
Steinmetz, M. O., Goldie, K. N. & Aebi, U. (1997). *J. Cell. Biol.* **138**, 559–574.
Weik, M., Ravelli, R. B. G., Kryger, G., McSweeney, S., Raves, M. L., Harel, M., Gros, P., Silman, I., Kroon, J. & Sussman, J. L. (2000). *Proc. Natl Acad. Sci. USA*, **97**, 623–628.
Yarmola, E. G., Somasundaram, T., Boring, T. A., Spector, I. & Bubb, M. R. (2000). *J. Biol. Chem.* **275**, 28120–28127.
Yeates, T. O. (1988). *Acta Cryst.* A**44**, 143–144.
Yeates, T. O. (1997). *Methods Enzymol.* **276**, 345–358.